

Fast model-based T_2 mapping using SAR-reduced simultaneous multislice excitation

Tom Hilbert^{1,2,3}  | Jenni Schulz⁴ | José P. Marques⁴  | Jean-Philippe Thiran^{2,3} |
Gunnar Krueger⁵ | David G. Norris⁴  | Tobias Kober^{1,2,3} 

¹Advanced Clinical Imaging Technology, Siemens Healthcare, Lausanne, Switzerland

²Department of Radiology, Lausanne University Hospital, Lausanne, Switzerland

³Signal Processing Laboratory 5, École Polytechnique Fédérale de Lausanne, Lausanne, Switzerland

⁴Donders Institute for Brain, Cognition and Behavior, Radboud University Nijmegen, Nijmegen, Netherlands

⁵Technology and Innovation, EMEA, Siemens Healthcare, Lausanne, Switzerland

Correspondence

Tom Hilbert, Siemens Healthineers, EPFL
Innovation Park QI-E, 1015 Lausanne,
Switzerland.

Email: tom.hilbert@epfl.ch

Twitter: @TomHilbertMRI

Purpose: To obtain whole-brain high-resolution T_2 maps in 2 minutes by combining simultaneous multislice excitation and low-power PINS (power independent of number of slices) refocusing pulses with undersampling and a model-based reconstruction.

Methods: A multi-echo spin-echo sequence was modified to acquire multiple slices simultaneously, ensuring low specific absorption rate requirements. In addition, the acquisition was undersampled to achieve further acceleration. Data were reconstructed by subsequently applying parallel imaging to separate signals from different slices, and a model-based reconstruction to estimate quantitative T_2 from the undersampled data. The signal model used is based on extended phase graph simulations that also account for nonideal slice profiles and B_1 inhomogeneity. In vivo experiments with 3 healthy subjects were performed to compare accelerated T_2 maps to fully sampled single-slice acquisitions. The accuracy of the T_2 values was assessed with phantom experiments by comparing the T_2 values to single-echo spin-echo measurements.

Results: In vivo results showed that conventional multi-echo spin-echo, simultaneous multislice, and undersampling result in similar mean T_2 values within regions of interest. However, combining simultaneous multislice and undersampling results in higher SDs (about 7 ms) in comparison to a conventional sequence (about 3 ms). The T_2 values were reproducible between scan and rescan ($SD < 1.2$ ms) within subjects and were in similar ranges across subjects ($SD < 4.5$ ms).

Conclusion: The proposed method is a fast T_2 mapping technique that enables whole-brain acquisitions at 0.7-mm in-plane resolution, 3-mm slice thickness, and low specific absorption rate in 2 minutes.

KEYWORDS

model-based reconstruction, simultaneous multislice, T_2 mapping

1 | INTRODUCTION

Quantitative MRI aims at measuring physical tissue properties directly, ideally independently from other physiological or technical influences. This allows for better comparability, both for longitudinal assessment within a patient, and across patients and imaging centers. Quantitative measures like relaxation, diffusivity, volumetry and myelin-water fraction, to name a few, have been used as quantitative biomarkers to indicate pathological processes.¹ In particular, T_2 has been shown to be sensitive to intracellular and extracellular water accumulation (i.e., a result of gliosis and edema) and myelin loss in the human brain.² This sensitivity has already been exploited in clinical applications such as ischemic stroke,³ peritumoral edema in malignant gliomas,⁴ and ischemic penumbra after thrombectomy,⁵ among others.

Traditionally, T_2 is determined using a Carr-Purcell-Meiboom-Gill (CPMG)⁶ sequence. To that end, multiple 180° refocusing pulses are applied after one 90° excitation pulse to generate multiple echoes. Over this train of spin echoes, the excited magnetization decays due to spin-spin interactions, which can be most simply modeled by a mono-exponential decay. However, due to imperfections of the applied refocusing pulses in CPMG-type sequences, not only the intended spin-echo signal pathways are created, but also stimulated echoes. Notably, stimulated echoes are always present in a CPMG sequence due to B_1 inhomogeneity and nonideal (i.e., not rectangular) slice profiles. If a mono-exponential decay is fitted over the different echoes, the resulting T_2 value will be overestimated. It is therefore common practice to ignore the first pure spin echo during the fitting; this widely used heuristic^{7,8} results in reproducible, but systematically biased T_2 estimates.⁹ To overcome this bias, Neumann et al suggested to correct this systematic bias retrospectively by approximating the overestimation depending on T_2 , B_1 , and sequence parameters using numerical simulations.¹⁰ Similarly, it was proposed to fit the signal model for stimulated echoes to the corrupted decay using either an analytical approximation^{11,12} or fitting of signal simulations.^{13,14}

T_2 mapping has very rarely been adopted for clinical routine, one of the main obstacles being the long acquisition time that the classical CPMG sequence requires. In recent years, various methods were published to accelerate the family of spin-echo sequences, such as by using different k-space reordering (RARE [rapid acquisition with refocused echoes]¹⁵) or sampling schemes (gradient and spin echo¹⁶). More generally, MRI sequences can be accelerated by undersampling k-space. An example is compressed sensing, which exploits the observation that MR images are compressible as prior knowledge in the reconstruction to recover missing samples.¹⁷ Compressed sensing approaches have been used to obtain

quantitative MRI maps, whereby the relaxation parameter to be measured provides an additional dimension upon which sparsity can be enforced (i.e., by applying total variation¹⁸ or locally low-rank regularization methods¹⁹). Similarly, model-based approaches exploit the parameter-encoding dimension by modeling the physical signal behavior and using this prior knowledge in an iterative reconstruction.^{7,12,20-23} However, the possibility of using high undersampling factors depends on the accuracy of the signal model, which may be violated by nonmodeled influences (e.g., blood flow, patient motion, B_1 inhomogeneity, and others).

One approach to accelerate 2D MRI sequences is to simultaneously acquire multiple slices (simultaneous multislice [SMS]) instead of only one.^{24,25} This is particularly useful from an SNR perspective when the 2D acquisitions have TRs significantly greater than the T_1 of the tissues of interest.²⁶ The SMS excitation pulses, in particular multiband (MB) pulses, are created by multiplexing sinc pulses, resulting in RF pulses that may be clipped due to higher RF amplitudes. Additionally, multiplexing results in a larger power deposition and hence restrictions due to specific absorption rate (SAR) safety constraints. This is especially the case for 180° multiplexed refocusing pulses, as used in T_2 mapping CPMG sequences; safety limits are easily reached that render the application of SMS refocusing for these types of sequences difficult for time-efficient protocols. This problem was addressed by power independent of number of slices (PINS) pulses.²⁷ The crucial difference of PINS to traditional SMS pulses is that they excite an infinite comb of slices (in reality limited by the transmit coil), but their power deposition is only approximately 2 times larger than that of 1 single sinc pulse. In practice, PINS pulses may affect areas of the body that are not within the intended FOV, as they excited an entire comb of slices. Therefore, transaxial slice orientations were not initially acquired. To enable axial acquisitions with CPMG sequences, a classical MB pulse can be used for excitation and PINS pulses only for refocusing.²⁸ In this configuration, PINS pulses have been used previously to accelerate acquisition times and reduce the power deposition of RARE²⁹ and half Fourier acquisition single-shot turbo spin-echo²⁸ sequences.

Shorter acquisition times are crucial for the adoption of quantitative MRI in clinical practice. This work addresses this problem by combining different acceleration approaches while accounting for systematic biases in the T_2 measurements, to obtain accurate and reproducible high-resolution T_2 maps of the whole brain in 2 minutes. To this end, we created a sequence that combines simultaneous slice excitation using PINS pulses with an acquisition scheme that exploits both traditional phase-encoding undersampling and TE undersampling.⁷ The reconstruction is model-based and accounts for the stimulated echoes.

2 | METHODS

2.1 | Sequence design

A standard CPMG sequence was modified to excite and receive the signal from multiple slices simultaneously. To this end, the standard excitation pulse (duration = 2.6 ms, bandwidth = 500 Hz) was replaced by a MB pulse (i.e., multiple multiplexed slice-selective pulses, duration = 3 ms, bandwidth = 800 Hz), and the standard refocusing pulses (duration = 3.8 ms, bandwidth = 666 Hz) were replaced by PINS pulses (duration = 3.8 ms, bandwidth = 260 Hz, 11 subpulses).²⁷ Following Schulz et al.,²⁸ the flip angles of the individual subpulses in the PINS pulse were iteratively optimized to yield an improved slice profile. Furthermore, gradient blips were added to the sequence to achieve controlled aliasing along the phase-encoding direction, depending on the slice location as previously reported.³⁰ Finally, as it is common practice, an interleaved slice sampling was used to acquire all different slice selections within a single TR. In the following, we will refer to this prototype design as the SMS-CPMG sequence. The corresponding sequence diagram is shown in Figure 1.

Furthermore, the sequence was undersampled using a block-sampling scheme as originally suggested in Sumpf et al.⁷ To that end, different phase-encoding gradients are played before and after each readout in the echo train. This individual phase encoding allows one to vary the sampling across echoes. Specifically, only a segment (block) of consecutive k-space lines is sampled in each echo, while the sampling blocks are shifted along the phase-encoding direction between echoes. Example sampling patterns for 60 phase-encoding steps, echo train length 16, and acceleration factors of 3 and 5 are shown in Figure 2. To ensure an equal distribution of sampling blocks within k-space, the following heuristic was used: (1) number of phase-encoding lines should be divisible by the undersampling factor, and (2) the undersampling factor itself should be an odd number, to avoid discontinuities at the center of k-space.

Before the modified CPMG sequence, a gradient-echo data set was automatically acquired (64×56 matrix, flip

angle = 8° , turbo factor = 64, TE = 1.47 ms, TR = 288 ms, acquisition time = 14 seconds), which sampled the reference lines to train the kernels for the slice-GRAPPA reconstruction.

2.2 | Reconstruction

All numerical simulations, data analysis, and visualizations were performed using MATLAB R2012a (The MathWorks, Natick, MA).

Data were reconstructed by subsequently applying a split-slice GRAPPA and a model-based iterative algorithm. First, GRAPPA kernels were trained on the external gradient-echo data. To have a fully sampled k-space, data from adjacent echoes were collapsed (i.e., assuming 3-fold k-space undersampling, undersampled data from 3 consecutive echoes were combined to form 1 fully sampled k-space, similar to multi-echo RARE images).¹⁵ The split-slice GRAPPA algorithm was then applied to the full k-space data sets as previously reported.³¹ Fully sampled RARE-type k-space data sets for each slice were thus obtained. Subsequently, the data for each slice were decollapsed to yield the same block-wise undersampled data structure as before, yet now for each slice. An illustration of the reconstruction pipeline and how data were collapsed is shown in Figure 3A.

At this point, the k-space data resemble a single-slice, block-undersampled data set, and any model-based reconstruction algorithm that can handle this sampling could be used to estimate T_2 (assuming a mono-exponential decay)⁷ or using a generating function that accounts for stimulated echoes.¹² However, the conjugate gradient algorithms used in these methods estimate T_2 and M_0 directly from k-space data using a single cost function. This cost function formulation is prone to converge to local minima. To achieve a stable convergence for a robust reconstruction of T_2 maps, additional measures must be taken, such as a gradient scaling to account for differences in the magnitude of T_2 and M_0 values or repeated restarts of the conjugate gradient algorithm. To

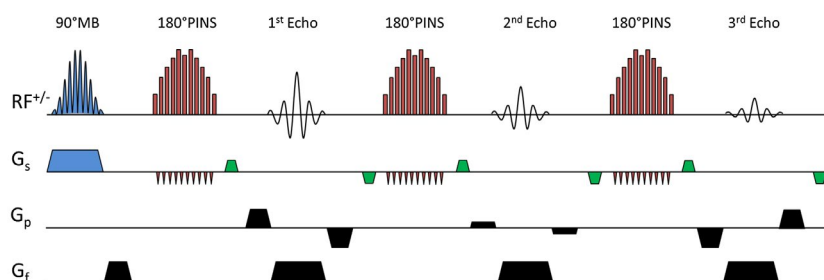


FIGURE 1 Carr-Purcell-Meiboom-Gill (CPMG) sequence diagram with transmit and receive RF ($RF^{+/-}$), slice-encoding, phase-encoding, and frequency-encoding gradients (G_s , G_p , and G_f). Excitation is performed with a multiband (MB) pulse and gradient (blue) and refocusing with PINS (power independent of number of slices) pulses (and its gradient blips [red]). Additionally, gradient blips (green) were added on top of the spoilers for controlled aliasing of slices along the phase-encoding direction

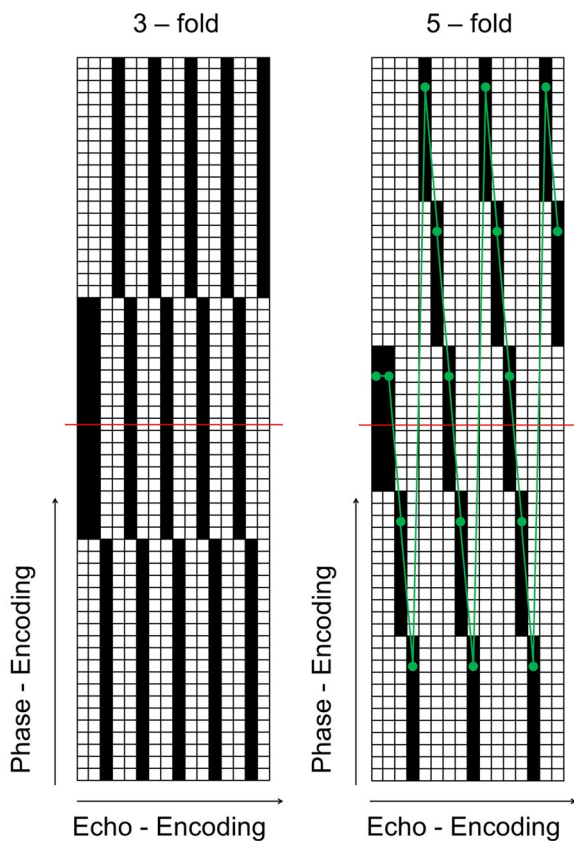


FIGURE 2 Example undersampling patterns for 3-fold and 5-fold acceleration with an echo train length of 16. White samples are skipped during acquisition, and black squares indicate the sampled k-space points. The red lines mark the k-space center (i.e., samples with zero phase encoding). Following Sumpf et al,¹² the k-space center was sampled in both first and second echo to improve the estimation with regard to B_1 variability. The green line in the 5-fold accelerated pattern shows an example trajectory of the third echo train (third TR) in that acquisition

avoid similar data-dependent measures, we propose a split algorithm similar to Huang et al.³² This algorithm will be referred to as “split algorithm for fast T_2 mapping” (SAFT).

SAFT splits the optimization problem into multiple sub-problems, resulting in a 3-step algorithm: Step A is optimizing the correspondence to the acquired data (data consistency); step B is optimizing the correspondence to the signal model (model consistency); and step C uses spatial regularization for a more robust reconstruction. These steps are iteratively repeated to estimate the free variables of the model (T_2 , B_1 , and M_0) and are explained in more detail in the following sections.

2.2.1 | Step A: Data consistency

The data consistency cost term models the imaging process including undersampling, Fourier transformation, and coil combination, and is similar to a typical conjugate gradient SENSE reconstruction with an additional term enforcing the signal

model onto the data. The images X at each TE are estimated by minimizing the difference to the k-space data Y as follows:

$$X = \underset{X}{\operatorname{argmin}} \frac{1}{2} \sum_{t \in TE} \left(\sum_{c=1}^N \|PF\{S_c X(t)\} - Y_{t,c}\|_2^2 + \alpha \|X(t) - \hat{X}(t)\|_2^2 \right), \quad (1)$$

where S are the complex coil sensitivities, N is the number of coils, F is the Fourier transform operator, and P is the sampling mask. The weight α enforces similarity to CPMG images \hat{X} , which are consistent with the signal model (i.e., images synthesized from the latest T_2 , B_1 , and M_0 estimates (see step B). Because \hat{X} is calculated only in the next step, the similarity weight α is set to zero to avoid any model influence in the first iteration.

2.2.2 | Step B: Signal model consistency

The model consistency cost term uses the current image estimate X from the data consistency (step A) to obtain the current best fit to the signal model. Theoretically, any signal model (e.g., analytical stimulated echo, Bloch simulations, mono-exponential decay) and any fitting method (e.g., dictionary, log linear, or least squares) can be used here. We decided to use the similar approach as MR fingerprinting^{33,34} (i.e., a dictionary fitting that matches the data to a model calculated using the extended phase graph [EPG³⁵] methodology, in which each echo was treated equally in the fitting). To that end, the EPG algorithm from Weigel et al³⁶ was used to simulate the CPMG signals for a range of T_2 values (128 values logarithmically spaced between 10 ms and 3000 ms), and B_1 efficiency factors in the interval of [0.60, 0.62, ..., 1.20] as well as a fixed $M_0 = 1$. Furthermore, different B_1 depositions due to imperfect slice profiles were accounted for by estimating 65 discrete bins (we chose a high number of bins to reduce granularity) of the profile for both the excitation and refocusing slice profiles with Bloch simulations (ignoring relaxation during the pulse). After simulating each bin, the signals were summed across the profile and stored in a dictionary together with the respective T_2 and B_1 used during simulation. Example slice profiles for the MB excitation, the PINS refocusing, and the standard CPMG pulses are shown in Figure 4 together with the simulated signals. To perform the fitting, a brute force search was used to find the best match for each voxel in image X with a simulated signal in the dictionary. The better the signal decay in the voxel matches a dictionary entry, the greater is the dot product between the 2 signal vectors. Therefore, the dictionary entry with the highest dot product is assumed to be the most representative for this voxel. As a result, the parameters that were used to simulate this entry can be attributed to this voxel. During the simulation of the dictionary entry, M_0 is fixed ($M_0 = 1$). Therefore, before calculating the dot product, the signals need to be normalized to account for

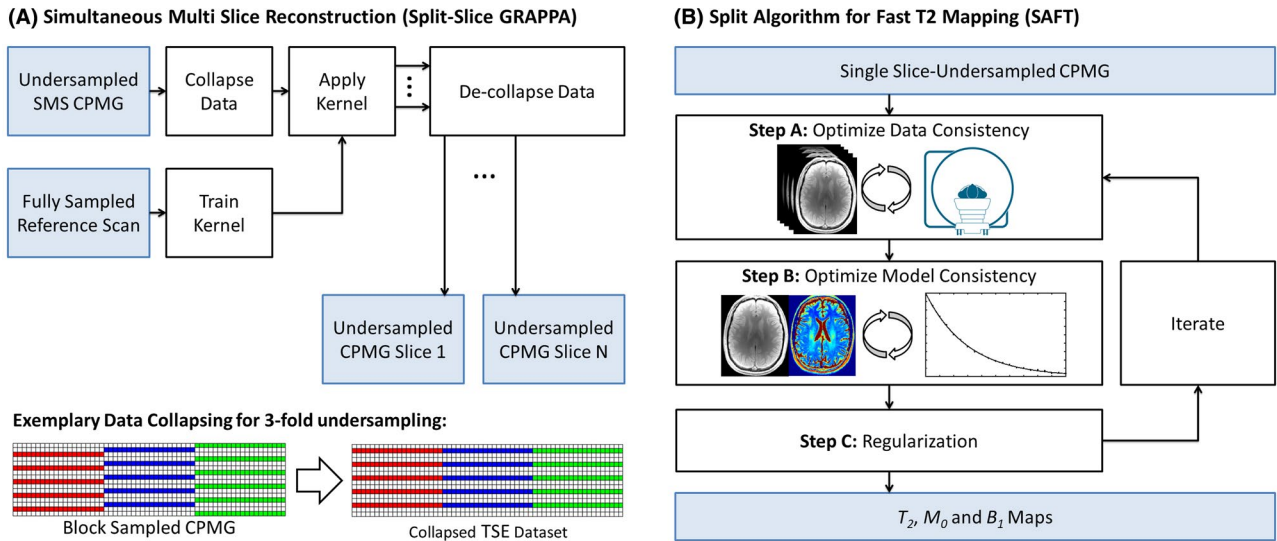


FIGURE 3 A, Application of split-slice GRAPPA on the undersampled k-space data to separate the signal from different slices. Before applying the kernel, the data-sampling blocks (red, blue, and green) from multiple echoes are collapsed to yield full k-space data. B, Model-based reconstruction that estimates T_2 , M_0 , and B_1 maps by iteratively improving data consistency, model consistency, and regularization. Abbreviations: SAFT, split algorithm for fast T_2 mapping; and TSE, turbo spin echo

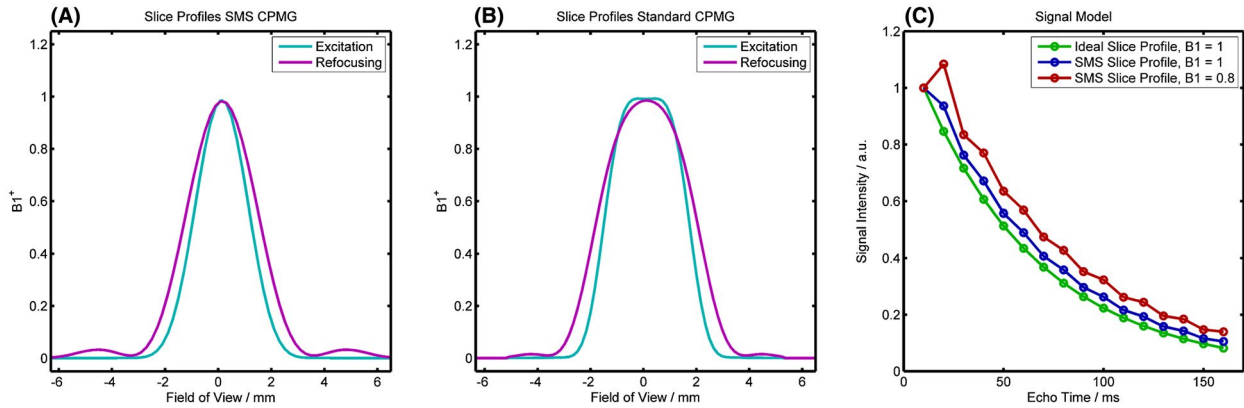


FIGURE 4 A, Slice profiles of the MB excitation (cyan) and PINS refocusing (purple) for 3-mm slice thickness. B, Slice profiles (excitation, cyan; refocusing, purple) for the standard CPMG sequence. C, Signals simulated with the extended phase graph (EPG) formalism for a CPMG sequence with $\Delta TE = 10$ ms and 16 echoes and tissue properties $T_2 = 60$ ms and $T_1 = 800$ ms with a rectangular slice profile (green) and the simultaneous multislice (SMS) slice profile without (blue) and with transmit field inhomogeneity (red)

variations in M_0 . Scaling factors are calculated using $s_{\text{sim}} = \|v_{\text{sim}}\|_2^{-1}$ for the signal in the dictionary entry and $s_{\text{acq}} = \|v_{\text{acq}}\|_2^{-1}$ for the acquired signal in the voxel, where v_{sim} and v_{acq} denote the discrete signal decays, respectively. The equilibrium magnetization is then estimated using these scaling factors following $M_0 = s_{\text{sim}} / s_{\text{acq}}$.

The entire process of Step B is comparable to maximizing the dot product between the CPMG images X and the simulated signals of the EPG sequence, depending on T_2 , M_0 , and B_1 :

$$\begin{pmatrix} T_2 \\ M_0 \\ B_1 \end{pmatrix} = \underset{T_2, M_0, B_1}{\text{argmax}} X \cdot M_0 \text{EPG}(T_2, B_1). \quad (2)$$

2.2.3 | Step C: Spatial regularization

In a last step, prior knowledge of the characteristics of the T_2 and B_1 maps is exploited to regularize the results obtained in the signal model consistency step (step B). The B_1 biases manifest themselves as smooth variations across the FOV. This is imposed on the obtained B_1 map by convolving it with a 2D Gaussian kernel G as follows:

$$B'_1 = B_1 * G(\sigma), \quad (3)$$

where σ is the SD of the kernel. Furthermore, we assume that the T_2 map is sparse in the Wavelet domain. Subsequent application of a Wavelet transform Ψ , a soft-threshold T with

strength λ , and the inverse Wavelet transform imposes this regularization:

$$T'_2 = \Psi^{-1} T(\Psi T_2, \lambda). \quad (4)$$

The equilibrium magnetization M_0 was not regularized, as experimental results (not shown) demonstrated a strong impact of M_0 regularization on the accuracy of the T_2 estimation (overestimation occurring with stronger regularization).

The regularized parameter maps T'_2 and B'_1 , together with M_0 (from step B), are used in the forward EPG signal model to calculate the CPMG images for all TEs $\hat{X}(t)$ based on the current (T'_2 , B'_1 , M_0) estimates:

$$\hat{X} = M_0 EPG(T'_2, B'_1). \quad (5)$$

The intensities of \hat{X} are model-consistent, as they were calculated using the numerical signal model (EPG simulation).

2.2.4 | Iterative loop and convergence

A new iteration is started by feeding the CPMG images \hat{X} , which were calculated based on the current estimate of T_2 , B_1 , and M_0 into the data consistency term (Equation 1) in step A. The similarity weighting α is set to a value greater than zero after the first iteration. The process of sequentially calculating steps A, B, and C is then repeated until a maximum number of iterations is reached.

For all reconstructions, a manually tuned Gaussian kernel ($\sigma = 3$ mm), Wavelet soft-threshold ($\lambda = 10$ ms), similarity weight ($\alpha = 1$), and 15 iterations were used. These values were determined experimentally before the reconstructions, based on the prior knowledge that B_1 is expected to be essentially linear within a radius of 3 mm and that we expect noise of the order of 10 ms for the T_2 map. The maximum number of iterations was determined by manually plotting the cost function and ensuring convergence.

2.3 | Acquisition

2.3.1 | In vivo studies

All measurements and calibrations were performed on a clinical 3T whole-body system (MAGNETOM Skyra; Siemens Healthcare, Erlangen, Germany) with actively shielded magnetic field gradient coils using a commercially available 64-channel head/neck coil. Before scanning, informed written consent was obtained from all volunteers, and the study was approved by the local ethics committee.

Data from 3 healthy volunteers were acquired using the proposed undersampled SMS-CPMG sequence (Figure 1) with a

slice acceleration factor of 5 (SMS = 5 [i.e., 5 slices acquired simultaneously]) and 3 different undersampling factors: $R = 1$ (i.e., fully sampled), $R = 3$, and $R = 5$. Relevant sequence parameters were as follows: TR = 3 seconds, 16 echoes with $\Delta TE = 10$ ms, matrix size = 320×210 , FOV = 220×192 mm², 50 slices, and 3-mm slice thickness with 0.3-mm slice gap. The acquisition times for the different combinations of acceleration factors resulted in 10:30 minutes for 5-fold (SMS \times R = 5×1) acceleration, 3:30 minutes for 15-fold (5×3) acceleration, and 2:06 minutes for 25-fold (5×5) acceleration. The measurement of the low-resolution gradient-echo sequence (matrix size = 64×64 , FOV = 220×192 mm²) required to calculate GRAPPA kernels added another 14 seconds of acquisition time. To study the reproducibility of the T_2 values, the 25-fold (5×5) accelerated acquisition was repeated without repositioning the volunteer to evaluate the scan-rescan variability of the T_2 values obtained in manually drawn regions of interest (ROIs).

For comparison, a fully sampled standard single-slice excitation CPMG sequence was acquired using the same sequence parameters, except for the number of slices, which had to be set to 10 to keep the same TR as in the prototype sequence. The acquisition time for this 10-slice comparison scan was 10:30 minutes. In theory, comparable slice coverage would result in a scan time of 52:30 minutes ($5 \times 10:30$ minutes) using the standard sequence. The T_2 maps from this standard CPMG sequence were estimated using the same iterative reconstruction as for the SMS-CPMG sequence.

To evaluate differences in T_2 caused by SMS, the standard CPMG and fully sampled SMS-CPMG T_2 maps were co-registered and their relative difference was calculated. Similarly, the relative T_2 difference maps were obtained from the fully sampled SMS sequence and the undersampled T_2 maps (after co-registration) to explore the differences due to the undersampling. Additionally, to visualize the goodness of fit, the residual of the data consistency term (Equation 1) was coil-combined using sum of squares and summed across echoes for the fully sampled acquisitions.

To compare the reproducibility of T_2 values in vivo across different degrees of acceleration and different subjects, ROIs were studied. To ensure reproducibility over the whole range of T_2 values found in the brain, the globus pallidus (GPA, exhibiting short T_2 values as a result of its high iron concentration³⁷) and the cortical spinal tracts (exhibiting long T_2 values as a result of the large-sized axons that tend to run parallel to the main magnetic field in the normal supine position³⁸) were studied. Additional ROIs were placed in the frontal lobe white matter (FWM), the thalamus, and splenium. All ROIs were manually drawn (T.H., MR physicist) bilaterally across multiple slices. The ROIs were placed within the FOV of the standard CPMG sequence to obtain reference values. Therefore, all T_2 values obtained from the SMS acquisitions originate from the central SMS slice, as

the CPMG sequence only acquires 10 slices in the center of the brain.

2.3.2 | Phantom studies

Phantom experiments were performed to quantitatively validate the T_2 values estimated with the proposed method. To that end, a multipurpose phantom (5 compartments with different concentrations of $\text{MnCl}_2 \cdot 4\text{H}_2\text{O}$ [Siemens E-38-19-195-K2130]) was scanned using the same protocols as in the in vivo studies. Additionally, multiple single-echo spin-echo acquisitions with different TEs (10 ms, 15 ms, 20 ms, 40 ms, 80 ms, and 150 ms) were performed to estimate the ground-truth T_2 values within the compartments using a nonlinear fit.

An additional phantom experiment was performed to study the impact of SMS on the estimated T_2 and B_1 values. Ideally, the estimated T_2 value should not depend on the SMS excitation profile (i.e., the T_2 value should be the same if it was excited/refocused with the central slice or 1 of the off-resonance slices within the comb of simultaneously acquired slices). To test this assumption, the fully sampled SMS-CPMG sequence was used to acquire data from the phantom 5 times (corresponding to the number of simultaneously acquired slices). Between acquisitions, the FOV was shifted along the slice direction by 33 mm (corresponding to the FOV in the slice direction divided by the number of simultaneous slices). In doing so, a single slice covering the compartments of the phantom was repeatedly acquired using the different slices within the SMS excitation profile. The T_2 and B_1 values estimated within the compartments, depending on the SMS slice, were extracted and compared in a bar graph.

2.4 | Simulations

The evolution of the T_2 decays are potentially affected by magnetization transfer (MT),³⁹ especially in white matter (WM), where short (myelin water) and long (intracellular and extracellular water) components are known to have different magnetization transfer properties.⁴⁰ This effect may lead to different T_2 decays for the SMS sequence in comparison to the standard CPMG sequence, as the used MB pulse saturates the semisolid pool with high pulse power at 5 different frequencies, and the PINS pulses always saturate the semisolid-pool on-resonance. To study this effect, we simulated the magnetization of the free water and semisolid pool for both the standard and the SMS-CPMG sequence in the presence of multiple components (i.e., intracellular/extracellular water [IE] and myelin [M] water) using the EPG-X framework.⁴¹ The magnetization was simulated for a central slice within the FOV, and the saturation caused by the acquisition of neighboring slices was considered. The following simulation parameters, similar to what could be expected in WM,⁴² were used: $T_{2,IE} = 60$ ms, $T_{2,M} = 10$ ms, $T_{2,Semi-Solid} = 12$ μ s,

$T_{1,IE} = 800$ ms, $T_{1,M} = 200$ ms, MT exchange rate $k_{IE} = 5$ s^{-1} , $k_M = 10$ s^{-1} , fractional MT pool size $F_{IE} = 10\%$, and $F_M = 30\%$. To simulate multiple T_2 components, the IE and M components were simulated separately and were subsequently summed. Therefore, exchange between components was not simulated. To simplify, the slice profile was ignored in this simulation, but a low $B_1 = 0.7$ was used. Using this simulation, 3 different T_2 decays were generated and compared between both sequences: no MT effect and no myelin, MT effect and no myelin, and MT effect and a myelin water fraction of 15%.

3 | RESULTS

3.1 | In vivo studies

The T_2 maps from the single-slice CPMG and the SMS-CPMG sequences with different acceleration factors are shown in Figure 5A. Note that the single-slice CPMG values are considered the gold standard measurement. A similar overall T_2 value range is observed in the SMS-CPMG maps compared with the gold standard. The maps from the accelerated slice-GRAPPA reconstruction with and without additional undersampling exhibit nonuniform noise amplification (Figure 5A). The relative difference maps (Figure 5B) do not show any contrast between WM and gray matter. However, differences in CSF are visible, whereas SMS resulted in higher T_2 values and undersampling results in lower T_2 values in CSF. The residual maps (Figure 5C) show mostly noise and residuals in the skull or in vessels (due to blood flow), which indicates that the signal model fitted the data well. Most notably, the SMS reconstruction introduces nonuniform noise amplifications with stronger noise in the center of the image and lower noise in the image corners, whereas the noise in the standard CPMG sequence is relatively uniform. These findings are supported by comparing T_2 values drawn from the ROIs (Figure 6). Overall, the mean values of the SMS-CPMG measurement are in good agreement; the acquisition of simultaneous multiple slices, however, introduces an increase in SD. For example, the T_2 values in the WM frontal lobe show a mean value of 68 ± 3.1 ms in single-slice CPMG versus 68.2 ± 6 ms in SMS CPMG. A slight additional increase in SD is observed in the undersampled SMS acquisitions, whereas the mean T_2 values stay in good agreement with the gold standard. There was no evidence of the acceleration being particularly unstable for either long or short T_2 values in the brain.

The FWM and GPA ROIs were used to compare T_2 values between scan and rescan within 1 subject and across subjects. The mean and SD in ROIs of the WM and GP for each subject between scans are shown in Figure 7. The T_2 values differ by 1 ms on average between scan and rescan and exhibit a low variation between scans (SD = 1.12 ms in FWM, 0.22 ms in GPA).

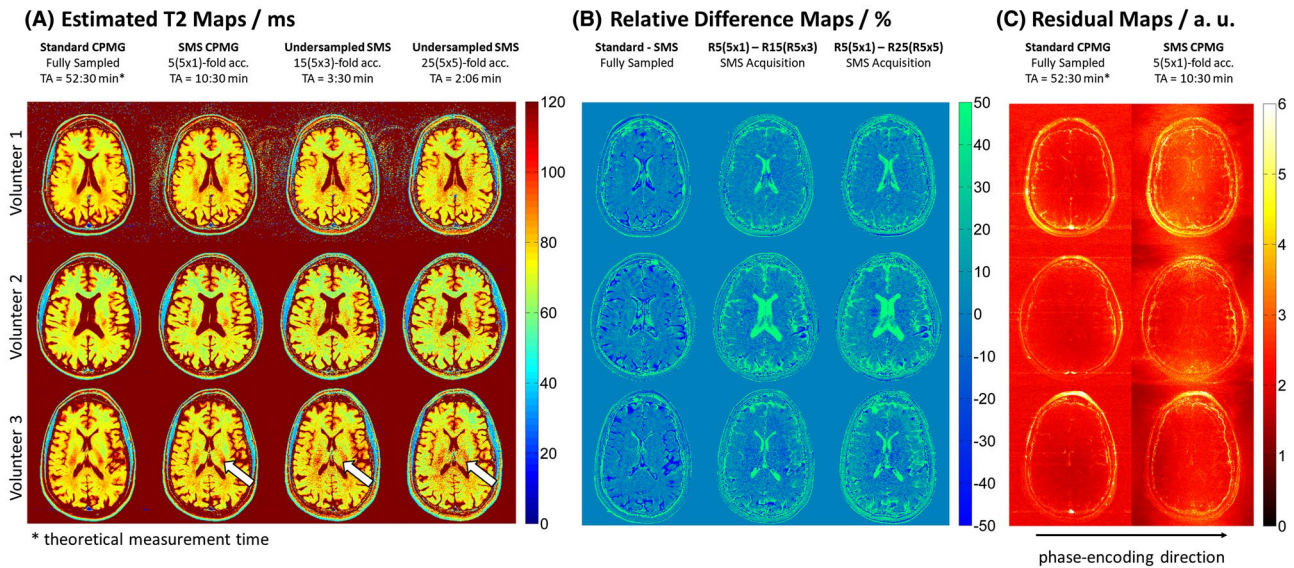


FIGURE 5 A, Axial slices from the T_2 maps of all volunteers that were reconstructed with the proposed method and acquired with different methods. Left to right: the gold-standard single-slice CPMG, SMS CPMG, and undersampled SMS CPMG ($R = 3$ and $R = 5$). Arrows indicate nonuniform noise amplifications. B, Relative differences in T_2 (after co-registration) between the standard sequence and the SMS sequence, to highlight the difference due to SMS, as well as difference maps between images acquired with different acceleration factors, to highlight differences due to undersampling. C, Residual maps indicating signal energy that could not be fitted to the EPG signal model used. Abbreviations: a.u., arbitrary units; and TA, acquisition time

The T_2 values across all subjects (within a similar age range of 27 ± 2 years) also show a small SD (4.16 ms in FWM, 4.08 in GPA). The remaining ROIs showed similar results, which are detailed in Supporting Information Figure S1.

3.2 | Phantom studies

Figure 8 shows an agreement plot of the T_2 values from the different accelerated acquisitions with T_2 values of the single-slice, single-spin-echo acquisition. All acquisitions agree well with the reference values. However, T_2 is slightly overestimated (~ 2 ms), especially for the undersampled acquisition and low T_2 values (< 30 ms). Furthermore, the SDs for low (< 20 ms) and high T_2 values (> 140 ms) are larger (~ 8 ms versus ~ 3 ms), presumably due to the fact that too few short TEs (for measuring low T_2 values) or too few long TEs (for long T_2 values) are sampled with the echo spacing and number of echoes used. How well the model fits the data can also be seen in Figure 8. The average signal intensity in the standard CPMG sequence within the compartments across echoes is plotted in comparison to the model of the signal corresponding to the mean T_2 and B_1 measured in that compartment. In general, the model fits the data well except for small differences in the signal intensities of the first and second echo.

Figure 9 shows the estimated T_2 and B_1 values depending on the slice within the SMS excitation profile. Throughout all compartments, the T_2 estimation based on the central (i.e., on-resonance) SMS slice shows the lowest T_2 value. In comparison, the estimated T_2 values from off-resonance slices are

longer, with the largest relative difference being 3.8% (in compartment 4). The estimated B_1 values appear to show larger differences (up to 8.2%), whereas the B_1 value appears to monotonically decrease when the FOV is moved from superior to inferior. We speculate that these differences are most likely caused by an imprecise excitation with the MB pulse.

3.3 | Simulations

Figure 10A shows an example magnetization for a simulation considering the MT effect. The semisolid pool (red) is saturated throughout the TR due to the acquisition of neighboring slices. This saturation is stronger for the SMS sequence, especially due to the MB excitation pulse, leading to a smaller longitudinal magnetization of both the free water and semisolid pools throughout the acquisition. However, the shape of the T_2 decay is not affected, and the normalized T_2 decays are almost identical between sequences (see Figure 10B for comparison). However, in the presence of multiple T_2 components, the longitudinal magnetization of these components will be affected differently due to different MT properties, leading to a small change in the early echoes of the T_2 decay, which depends on the pulse power used (see also Figure 10B for comparison).

3.4 | Specific absorption rate aspects

The main motivation for the proposed sequence design of using a classical MB excitation and PINS refocusing pulses was to obtain a CPMG sequence that is able to acquire many

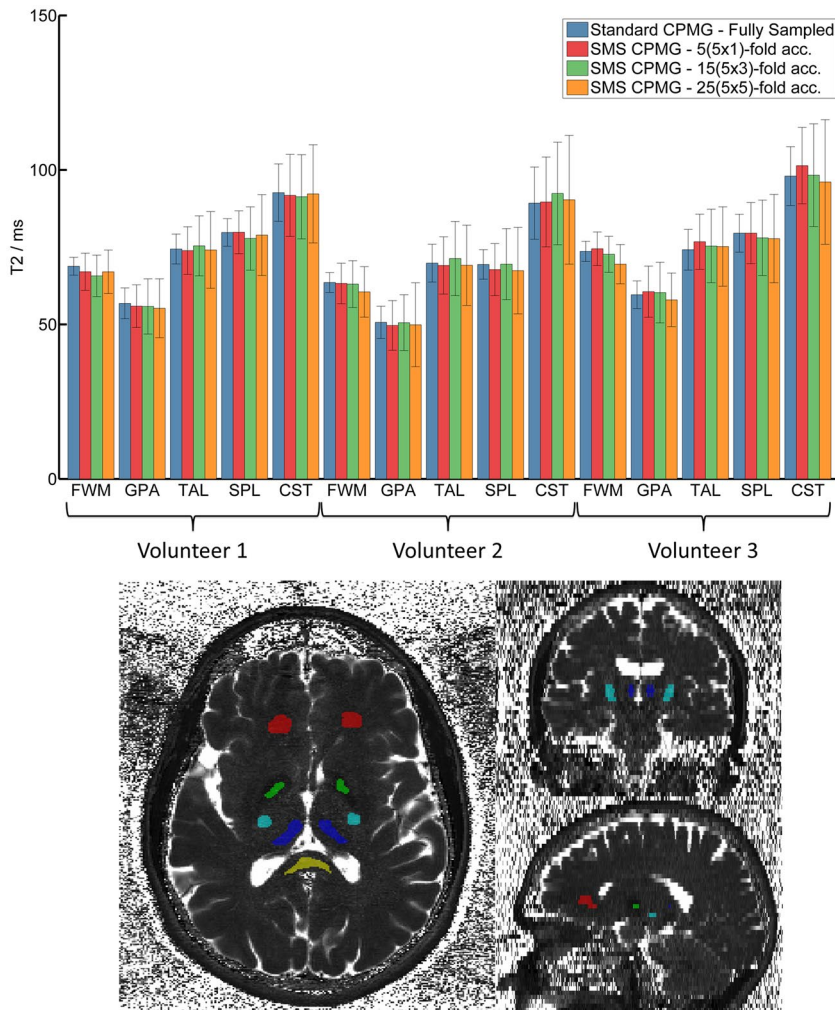


FIGURE 6 Top: Mean and SD of T_2 values (in milliseconds) within regions of interest (ROIs) that were manually drawn into the white matter of the frontal lobe (FWM), globus pallidus (GPA), thalamus (TAL), splenium (SPL), and cortical spinal tract (CST) for each subject and T_2 sequence. Bottom: Example ROIs are shown overlaid on a T_2 map for 1 subject, with the colors indicating the FWM (red), GPA (green), TAL (blue), SPL (yellow), and CST (turquoise)

slices (e.g., 50 for high-resolution whole-brain coverage) and echoes (e.g., 16) in a short TR (e.g., 3 seconds) without exceeding the SAR limitations. Pulse simulations were used to calculate the B_1 for every pulse and showed that the SAR reduction was achieved because the PINS refocusing pulses deposit similar power ($B_1 = 6.3 \text{ mT}^2$) in comparison to the standard single-slice refocusing pulse ($B_1^2 = 6.9 \text{ mT}^2$), although it refocuses 4 more slices. This low-power deposition of the PINS pulses facilitated the use of this sequence design despite the approximately 5-times higher B_1^2 of the multiband excitation (11.1 mT^2) in comparison to the single-slice excitation ($B_1^2 = 2.7 \text{ mT}^2$). With this configuration, the proposed SMS-CPMG sequence was on average at about 60% of the SAR limit for 50 slices during the in vivo experiments, based on the vendor's SAR model. In comparison, the single-slice excitation CPMG sequence reached about 40% of the SAR limit for the acquisition of only 10 slices.

3.5 | Computational requirements

The image reconstruction of 1 data set with 50 slices required approximately 7 hours on an office computer with 16 GB of

RAM and an Intel Core i7-3770K 3.5-GHz CPU running a 64-bit Windows 7 operating system.

The algorithm has its largest memory footprint when the split-slice GRAPPA kernel is applied and depends strongly on the matrix size of k-space. In the case of the in vivo experiments, this corresponds to approximately 5.5 GB (matrix size 320×210 , 16 echoes, 64 coils, 5 simultaneous slices). Notably, due to the collapsing of the undersampled k-space prior to the kernel application, the footprint is linearly reduced by the undersampling factor R .

4 | DISCUSSION

We have shown that the proposed multiband/PINS simultaneous multislice sequence design, combined with regular undersampling and an EPG signal model applied with dictionary fitting, yields accurate T_2 maps of the whole brain with a high resolution in 2 minutes.

The results show that the used slice-profile-sensitive EPG simulation takes the major artifactual effects on the signal into account, notably stimulated echoes originating

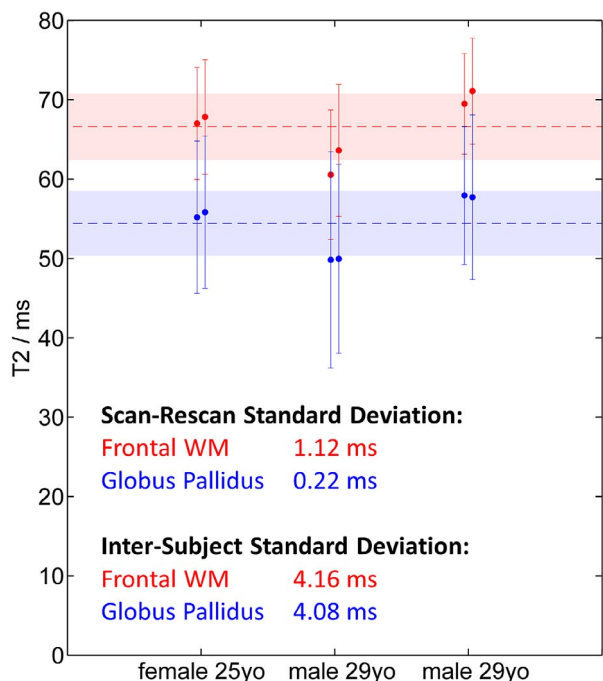


FIGURE 7 Mean T_2 values of scan and rescan with a slice acceleration factor of 5 and 5-fold undersampling for each subject with error bars indicating the SD. Red indicates values from the FWM, and blue indicates the GPA. The dashed lines indicate the mean across all subjects, and the filled area indicates the cross-subject SD

from incomplete refocusing of the spins that are inevitable due to B_1^+ field inhomogeneity and nonideal slice profiles. However, the model is still an approximation and does not account for the detailed microstructure of human tissue. One main assumption of the model used in this work is that it models only 1 compartment (i.e., 1 single isochromat with a specific T_2 relaxation time per voxel). This is obviously a

simplification and will not account for differently behaving compartments such as intracellular and extracellular water compartments. Ideally, the model should be extended to fully incorporate these effects and additional tissue properties; however, this will decrease the computational stability of the fitting and require either additional signal encoding or an optimized reconstruction to keep the same acquisition times. We speculate that a systematic error is introduced if the nonmodeled effects mimic signal behavior, which is describable by the model. For example, the apparent T_2 value in blood is higher than the actual T_2 value of blood, as flow causes a rapid exponential decay in the transverse magnetization. However, if the nonmodeled effect is causing signal behavior, which does not correspond to the model, the image quality of the reconstructed maps will decrease because the model is used as prior knowledge to cope with undersampling. For example, if the subject moves during the acquisition, the signal along the echo train will behave differently from a typical T_2 decay. This model violation will result in additional artifacts (on top of motion artifacts), as the missing k-space samples from the undersampling cannot be properly recovered. It should be noted, however, that despite these shortcomings, the T_2 values measured here are in good agreement with the gold-standard single-slice single-spin-echo acquisition. Furthermore, the T_2 values show only small differences between repeated measures using different slices of the SMS excitation profile.

The simulations demonstrated that the difference in pulse power between the standard and CPMG sequence only influences the initial magnetization and not the T_2 decay itself, if we assume a single T_2 component. Therefore, only the M_0 and not the T_2 estimation is affected. However, in the presence of multiple T_2 components, small differences can be observed in the T_2 decay, which may lead to

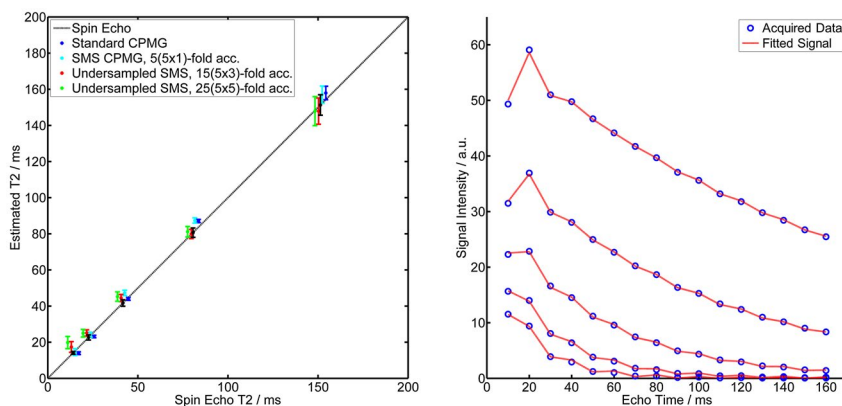


FIGURE 8 Left: Mean T_2 values within 5 different compartments of a phantom from the different acquisitions reconstructed with the proposed SAFT algorithm against the reference values derived from a spin-echo sequence. Error bars indicate the SD, and the markers were horizontally jittered to minimize overlaps. Right: Five standard CPMG decays corresponding to the 5 different compartments, with blue circles indicating the measured average signal intensity in each echo and compartment, and the red dotted line indicating the signal decay corresponding to the fitted T_2 and B_1 values within that compartment

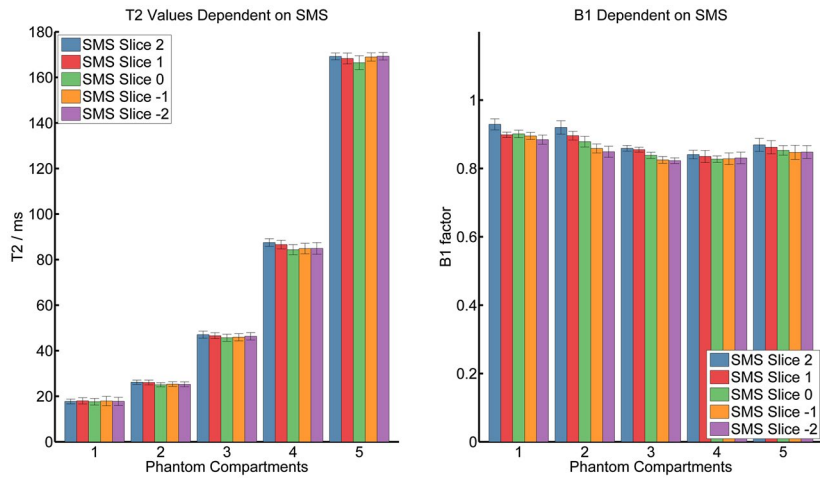
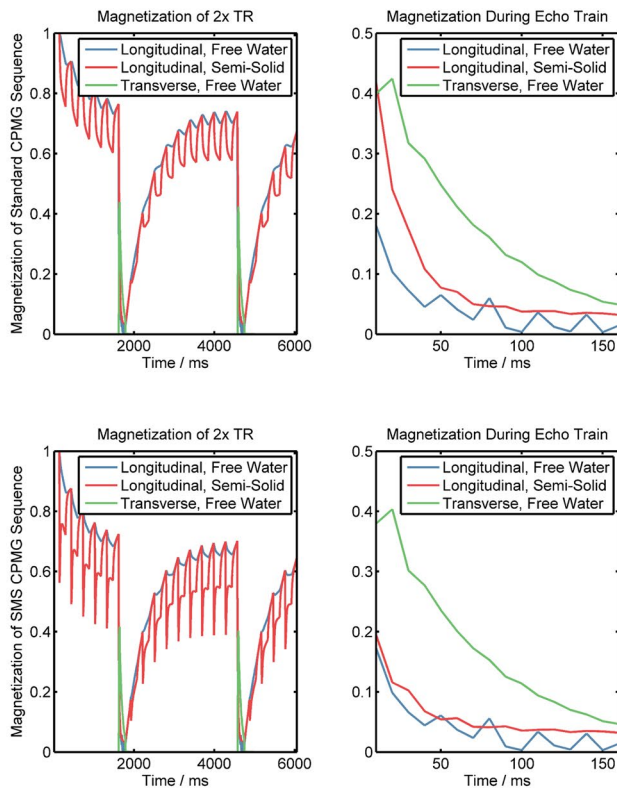


FIGURE 9 Estimated quantitative T_2 and B_1 values within the compartments of a phantom, dependent on which slice from the comb of simultaneously acquired slices is used to measure the echo train. “Slice 0” indicates the center slice, and “Slice 1, 2, -1, -2” indicate the respective off-resonance slices

(A) Comparison of Standard and SMS CPMG Magnetization



(B) T2 Decays Depending on Sequence, MT, and MWF

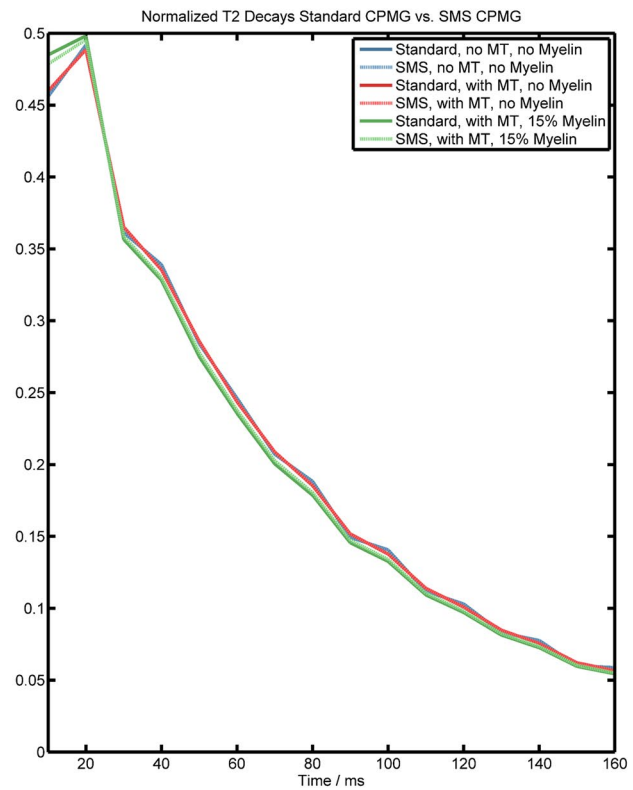


FIGURE 10 A, Magnetization of the standard (top) and the SMS (bottom) CPMG sequences over the course of 2 TRs (left) and zoomed into the T_2 decay of the second TR (right). B, Normalized T_2 decays from both the standard and SMS-CPMG sequence without magnetization transfer (MT) effect and no myelin, with MT effect and no myelin, and with MT effect and a myelin water fraction (MWF) of 15%

an overestimation of T_2 depending on the pulse power used. However, we assume that this effect is small, as no contrast between WM (strong MT) and gray matter (weak MT) was observed in the relative difference and residual maps. A more detailed analysis of MT effects in CPMG acquisitions can be found in Radunsky et al.⁴³

When accelerating, both SMS and the additional undersampling result in amplification of noise, which manifests itself in

increasing SDs at higher acceleration factors. Nevertheless, the accuracy of the estimation remains unbiased. Despite the increased SDs, T_2 values were reproducible in scan–rescan acquisitions and across subjects (SD = 1.12 ms in FWM, 0.22 ms in GPA). This is an important observation, as reproducibility is an important aspect in a clinical context. For example, in follow-up measurements of multiple sclerosis, T_2 maps have to be comparable and even small changes might indicate pathology,

such as an increased inflammation of the “normal appearing white matter,” which is very hard to observe with the naked eye.

The original motivation of using PINS pulses instead of multiband pulses were the SAR limitations, which especially come into play at 3 T: the application of multiple 180° RF pulses easily exceeds the SAR limits, even with conventional single-slice acquisitions. We demonstrated that the power deposition per slice is significantly lower with the proposed pulse scheme, enabling the use of such pulse schemes greater than 1.5 T. Such a scheme may enable using spin-echo-based T_2 mapping at ultrahigh fields (i.e., 7 T and beyond).²⁹

When doing standard interleaved multislice CPMG, 1 main drawback of acquiring a large number of slices is the extremely long TR. If the same volume acceleration as in the SMS acquisition was intended, as with an interleaved multislice excitation, a TR of about 15 seconds would have to be used, rendering the sequence highly SNR inefficient. In such situations, SMS is highly beneficial and, in theory, a TR of 1 second could be used (approximately $1.2 \times T_1$ of a relevant tissue, such as WM with a T_1 of about 800 ms). In the current SMS-CPMG implementation with interleaved slice sampling, the continuous application of the refocusing pulse has a saturation effect in neighboring slices because of the poor slice profile of both the excitation and refocusing pulses; therefore, this saturation was mitigated by choosing a longer TR of 3 seconds. In the future, this additional idle time in the sequence design may be used to acquire a longer echo train (e.g., 32 echoes) in clinical applications with long T_2 values (e.g., neonate brain, abdominal imaging). In a similar context, there may be remaining MT effects, as the interleaved slice sampling also corresponds to a continuous saturation of the semisolid water pool at different off-center frequencies.⁴⁴ This saturation will be different for a conventional CPMG in comparison to the SMS CPMG and may be the cause for small difference when comparing T_2 values from the 2 methods.

One major limitation of the proposed method is that the reconstruction algorithm is rather complex in comparison to a direct Fourier transform and mono-exponential fitting. This complexity involves multiple regularization parameters (α , λ , and σ) and leads to rather long computational times of about 7 hours on a desktop computer. The regularization parameters were optimized manually, as is common practice in compressed sensing.^{17,32} In future work, these parameters should be automatically adapted, also depending on image content. The long computational time of the reconstruction algorithm still prohibits its use in clinical routine. However, the performance of the current implementation can certainly be improved through code optimization, parallelization across slices, and hardware acceleration on an image reconstruction server. Future work may also use the B_1 value measured with an additional rapid B_1 mapping sequence within the reconstruction to reduce complexity and thus improve robustness.

Following a prominent trend in today’s research community, the reconstruction may also be performed using convolutional neuronal networks or similar approaches (sometimes referred to as artificial intelligence), which may result in faster reconstruction times.^{45,46}

An alternative combination of SMS and model-based reconstruction could be realized by solving it as a single inverse problem rather than 2 subsequently applied reconstructions. To achieve this, it would be necessary to also model the aliasing of the simultaneously acquired slices and their respective coil sensitivities within the data consistency term (Equation 1). However, we avoided this approach, as this would further increase the computational costs and we also assume that combining the reconstruction into a single inverse problem may result in a worse artifact behavior and robustness toward model violations (e.g., blood flow, inaccurate coil sensitivities).

In future work, multi-PINS pulses (a combination of multi-PINS pulses)⁴⁷ should be explored for quantitative mapping. These pulses may allow a reduction in the slice thickness without worsening the slice profile. Furthermore, applying a wave gradient during readout⁴⁸ could help to further reduce interslice leakage in the slice-GRAPPA reconstruction and should also be explored.

Undersampled SMS CPMG may be used to explore other clinical applications of quantitative T_2 mapping in a standard clinical setting. For example, in abdominal imaging, a greater number of slices could be acquired within a single breath-hold, or even during a free-breathing sequence that is triggered to acquire multiple slices at end-expiration. However, we only demonstrated a proof of concept here, and larger clinical studies are required to further validate the T_2 values.

5 | CONCLUSIONS

A new sequence design was proposed that enables undersampled SMS-CPMG acquisitions at 3 T without exceeding the SAR limits. The proposed combination of split-slice GRAPPA and a model-based reconstruction that accounts for stimulated echoes resulted in accurate and reproducible T_2 values in phantom and in in vivo experiments.

CONFLICT OF INTEREST

Tom Hilbert, Gunnar Krueger, and Tobias Kober are employed by Siemens Healthcare, Switzerland.

ORCID

Tom Hilbert  <https://orcid.org/0000-0001-8207-4908>

José P. Marques  <https://orcid.org/0000-0001-8157-8864>

David G. Norris  <https://orcid.org/0000-0002-3699-6917>

Tobias Kober  <https://orcid.org/0000-0001-7598-9456>

REFERENCES

- Deoni S. Quantitative relaxometry of the brain. *Top Magn Reson Imaging*. 2010;21:101–113.
- Helms G. Tissue properties from quantitative MRI. In: Toga AW, ed. *Brain Mapping*. Waltham, MA: Academic Press; 2015:287–294.
- Siemonsen S, Mouridsen K, Holst B, et al. Quantitative T2 values predict time from symptom onset in acute stroke patients. *Stroke*. 2009;40:1612–1616.
- Blystad I, Marcel Warntjes JB, Smedby O, Lundberg P, Larsson EM, Tisell A. Quantitative MRI for analysis of peritumoral edema in malignant gliomas. *PLoS ONE*. 2017;12:e0177135.
- Seiler A, Lauer A, Deichmann R, et al. Complete restitution of the ischemic penumbra after successful thrombectomy: a pilot study using quantitative MRI. *Clin Neuroradiol*. 2018;1–9.
- Meiboom S, Gill D. Modified spin-echo method for measuring nuclear relaxation times. *Rev Sci Instrum*. 1958;29:688–691.
- Sumpf TJ, Uecker M, Boretius S, Frahm J. Model-based nonlinear inverse reconstruction for T2 mapping using highly undersampled spin-echo MRI. *J Magn Reson Imaging*. 2011;34:420–428.
- Smith HE, Mosher TJ, Dardzinski BJ, et al. Spatial variation in cartilage T2 of the knee. *J Magn Reson Imaging*. 2001;14:50–55.
- McPhee KC, Wilman AH. Limitations of skipping echoes for exponential T2 fitting. *J Magn Reson Imaging*. 2018;48:1432–1440.
- Neumann D, Blaimer M, Jakob PM, Breuer FA. Simple recipe for accurate T2 quantification with multi spin-echo acquisitions. *Magn Reson Mater Physics, Biol Med*. 2014;27:567–577.
- Lukzen NN, Petrova MV, Koptyug IV, Savelov AA, Sagdeev RZ, Petrova MV, Koptyug IV, Savelov AA, Sagdeev RZ. The generating functions formalism for the analysis of spin response to the periodic trains of RF pulses. Echo sequences with arbitrary refocusing angles and resonance offsets. *J Magn Reson*. 2009;196:164–169.
- Sumpf TJ, Petrovic A, Uecker M, Knoll F, Frahm J. Fast T2 mapping with improved accuracy using undersampled spin-echo MRI and model-based reconstructions with a generating function. *IEEE Trans Med Imaging*. 2014;33:2213–2222.
- Lebel RM, Wilman AH. Transverse relaxometry with stimulated echo compensation. *Magn Reson Med*. 2010;64:1005–1014.
- Ben-Eliezer N, Sodickson DK, Block KT. Rapid and accurate T2 mapping from multi-spin-echo data using bloch-simulation-based reconstruction. *Magn Reson Med*. 2015;73:809–817.
- Hennig J, Nauwerth A, Friedburg H. RARE imaging: a fast imaging method for clinical MR. *Magn Reson Med*. 1986;3:823–833.
- Oshio K, Feinberg DA. GRASE (gradient- and spin-echo) imaging: a novel fast MRI technique. *Magn Reson Med*. 1991;20:344–349.
- Lustig M, Donoho D, Pauly JM. Sparse MRI: the application of compressed sensing for rapid MR imaging. *Magn Reson Med*. 2007;58:1182–1195.
- Velikina JV, Alexander AL, Samsonov A. Accelerating MR parameter mapping using sparsity-promoting regularization in parametric dimension. *Magn Reson Med*. 2013;70:1263–1273.
- Zhang T, Pauly JM, Levesque IR. Accelerating parameter mapping with a locally low rank constraint. *Magn Reson Med*. 2015;73:655–661.
- Doneva M, Börnert P, Eggers H, Stehning C, Sénégas J, Mertins A. Compressed sensing reconstruction for magnetic resonance parameter mapping. *Magn Reson Med*. 2010;64:1114–1120.
- Block KT, Uecker M, Frahm J. Model-based iterative reconstruction for radial fast spin-echo MRI. *IEEE Trans Med Imaging*. 2009;28:1759–1769.
- Tran-Gia J, Wech T, Bley T, Köstler H. Model-based acceleration of Look-Locker T1 mapping. *PLoS ONE*. 2015;10:e0122611.
- Wang X, Roeloffs V, Klosowski J, et al. Model-based T1 mapping with sparsity constraints using single-shot inversion-recovery radial FLASH. *Magn Reson Med*. 2017;79:730–740.
- Larkman DJ, Hajnal JV, Herlihy AH, Coutts GA, Young IR, Ehnholm G. Use of multicoil arrays for separation of signal from multiple slices simultaneously excited. *J Magn Reson Imaging*. 2001;13:313–317.
- Barth M, Breuer F, Koopmans PJ, Norris DG, Poser BA. Simultaneous multislice (SMS) imaging techniques. *Magn Reson Med*. 2016;75:63–81.
- Marques JP, Norris DG. How to choose the right MR sequence for your research question at 7 T and above? *NeuroImage*. 2018;168:119–140.
- Norris DG, Koopmans PJ, Boyacıoğlu R, Barth M. Power independent of number of slices (PINS) radiofrequency pulses for low-power simultaneous multislice excitation. *Magn Reson Med*. 2011;66:1234–1240.
- Schulz J, P. Marques J, ter Telgte A, et al. Clinical application of Half Fourier Acquisition Single Shot Turbo Spin Echo (HASTE) imaging accelerated by simultaneous multi-slice acquisition. *Eur J Radiol*. 2018;98:200–206.
- Norris DG, Boyacıoğlu R, Schulz J, Barth M, Koopmans PJ. Application of PINS radiofrequency pulses to reduce power deposition in RARE/turbo spin echo imaging of the human head. *Magn Reson Med*. 2014;71:44–49.
- Setsompop K, Gagoski BA, Polimeni JR, Witzel T, Wedeen VJ, Wald LL. Blipped-controlled aliasing in parallel imaging for simultaneous multislice echo planar imaging with reduced g-factor penalty. *Magn Reson Med*. 2012;67:1210–1224.
- Cauley SF, Polimeni JR, Bhat H, Wald LL, Setsompop K. Interslice leakage artifact reduction technique for simultaneous multislice acquisitions. *Magn Reson Med*. 2014;72:93–102.
- Huang F, Chen Y, Yin W, et al. A rapid and robust numerical algorithm for sensitivity encoding with sparsity constraints: self-feeding sparse SENSE. *Magn Reson Med*. 2010;64:1078–1088.
- Ma D, Gulani V, Seiberlich N, et al. Magnetic resonance fingerprinting. *Nature*. 2013;495:187–192.
- Cloos MA, Knoll F, Zhao T, et al. Multiparametric imaging with heterogeneous radiofrequency fields. *Nat Commun*. 2016;7:12445.
- Hennig J, Weigel M, Scheffler K. Calculation of flip angles for echo trains with predefined amplitudes with the extended phase graph (EPG) algorithm: principles and applications to hyperecho and TRAPS sequences. *Magn Reson Med*. 2004;51:68–80.
- Weigel M. Extended phase graphs: dephasing, RF pulses, and echoes—pure and simple. *J Magn Reson Imaging*. 2015;41:266–295.
- Bartzokis G, Sultzer D, Mintz J, et al. In vivo evaluation of brain iron in Alzheimer's disease and normal subjects using MRI. *Biol Psychiatry*. 1994;35:480–487.
- Gil R, Khabipova D, Zwiers M, Hilbert T, Kober T, Marques JP. An in vivo study of the orientation-dependent and independent components of transverse relaxation rates in white matter. *NMR Biomed*. 2016;29:1780–1790.

39. Henkelman RM, Stanisz GJ, Graham SJ. Magnetization transfer in MRI: a review. *NMR Biomed*. 2001;14:57–64.
40. Vavasour IM, Whittall KP, Li D, MacKay AL. Different magnetization transfer effects exhibited by the short and long T2 components in human brain. *Magn Reson Med*. 2000;44:860–866.
41. Malik SJ, Teixeira R, Hajnal JV. Extended phase graph formalism for systems with magnetization transfer and exchange. *Magn Reson Med*. 2018;80:767–779.
42. Gloor M, Scheffler K, Bieri O. Quantitative magnetization transfer imaging using balanced SSFP. *Magn Reson Med*. 2008;60:691–700.
43. Radunsky D, Blumenfeld-Katzir T, Volovyk O, et al. Analysis of magnetization transfer (MT) influence on quantitative mapping of T2 relaxation time. *Magn Reson Med*. 2019;82:145–158.
44. Santyr GE. Magnetization transfer effects in multislice MR imaging. *Magn Reson Imaging*. 1993;11:521–532.
45. Hammernik K, Klatzer T, Kobler E, et al. Learning a variational network for reconstruction of accelerated MRI data. *Magn Reson Med*. 2018;79:3055–3071.
46. Zhu B, Liu JZ, Cauley SF, Rosen BR, Rosen MS. Image reconstruction by domain-transform manifold learning. *Nature*. 2018;555:487.
47. Eichner C, Wald LL, Setsompop K. A low power radiofrequency pulse for simultaneous multislice excitation and refocusing. *Magn Reson Med*. 2014;72:949–958.
48. Gagoski BA, Bilgic B, Eichner C, et al. RARE/turbo spin echo imaging with simultaneous multislice wave-CAIPI. *Magn Reson Med*. 2015;73:929–938.

SUPPORTING INFORMATION

Additional supporting information may be found online in the Supporting Information section at the end of the article.

FIGURE S1 Mean T_2 values of scan and rescan with a slice acceleration factor of 5 and 5-fold undersampling for each subject, with error bars indicating the SD in various brain regions. The dashed lines indicate the mean across all subjects, and the filled area indicates the cross-subject SD

How to cite this article: Hilbert T, Schulz J, Marques JP, et al. Fast model-based T_2 mapping using SAR-reduced simultaneous multislice excitation. *Magn Reson Med*. 2019;82:2090–2103.
<https://doi.org/10.1002/mrm.27890>